AIAA JOURNAL
Vol. 35, No. 2, February 1997

Stability of a Counter-Rotating Vortex Pair Immersed in Cross-Stream Shear Flow

J. S. Marshall* and H. Chen†
University of Iowa, Iowa City, Iowa 52242-1585

The three-dimensional stability and nonlinear evolution of a single vortex and a pair of vortices of opposite strength immersed in a weak cross-stream shear flow are examined. The shear flow rate S is assumed to be sufficiently small compared to the average core vorticity $\Gamma/\pi\sigma^2$ that the vortex cross sections are nearly circular and the effect of stretching of the background shear flow is negligible, while being sufficiently large compared to the vortex mutual interaction frequency $\Gamma/2\pi b^2$ to significantly influence the stability of the vortex pair. The effect of shear flow on the long- and short-wave instabilities are studied using a combination of linear theory and numerical simulations for nonlinear disturbances. The presence of cross-stream shear is found to introduce a coupling between the symmetric and antisymmetric perturbation modes of the vortex pair, which leads to the development of three distinctly different types of long-wave vortex instabilities. One type of instability is dominated by the interaction of the vortex self-induced velocity with the shear flow. The second type of instability is dominated by interaction of the vortices with each other. In the third type of instability, both the shear flow and the mutual interaction of the vortices are important. The nonlinear evolution of the vortex pair is qualitatively different for each of these three cases. For short-wave perturbations, the presence of cross-stream shear is found to increase the growth rate and wave-number range of the unstable perturbations, provided that the shearing rate is sufficiently large.

Nomenclature

b	= vortex nominal separation distance
C	= vortex centerline
e	= equivalent straining rate, $e \equiv \Gamma/2\pi b^2$
f_n	= weighting function of element n
$\boldsymbol{G}_n$	= amplitude of element n
k	= perturbation wave number
R_n	= radius of element n
$\boldsymbol{r}$	= position vector to vortex centerline
S	= shearing rate
$\boldsymbol{u}_I$, $\boldsymbol{u}_E$	= vorticity-induced and shear-flow velocities
$\boldsymbol{W}$	= vorticity of ambient shear flow
$\boldsymbol{x}$	= position vector to any point in three-dimensional space
$\boldsymbol{x}_n$	= position vector of element point n
y, z	= perturbations of vortex centerline
α	= growth rate
β	= dimensionless vortex separation distance, $\beta \equiv bk$
Γ	= vortex circulation
δ	= dimensionless vortex core radius, $\delta \equiv \sigma k$
δ_c, δ_R	= Crow and Rosenhead cutoff constants
$\bar{\delta}$	= cutoff distance, $\bar{\delta} \equiv \delta_c \sigma k$
ξ	= Lagrangian position of particle on vortex axis
σ	= vortex core radius
Ψ, χ	= mutual induction functions
Ω_n	= self-induced rotation rate of mode n perturbation
ω	= self induction function $[\omega(\bar{\delta}) \equiv -(2/\bar{\delta}^2)\Omega_n^*(\bar{\delta})]$
ω	= vorticity vector

Subscripts

A	= antisymmetric mode
f	= fastest-growing perturbations
S	= symmetric mode

Superscript

$*$	= variable nondimensionalized by $\Gamma/\pi\sigma^2$

I. Introduction

THE presence of nominally parallel vortices with opposite circulation is a dominant feature in the wake behind most lifting bodies, including airplanes, submarines, hydrofoil craft, and automobiles. These vortices exhibit well-known long-wave and short-wave instabilities,[1] with wave number k satisfying $k\sigma \ll 1$ and $k\sigma = O(1)$, respectively. The effects of these instabilities are readily observable, for instance, in oscillations of the trailing vortices behind large aircraft under suitable atmospheric conditions. The existence of the trailing vortices is responsible for a number of important effects. For instance, passage of aircraft through the trailing vortices of preceding aircraft is a significant cause of loss of vehicle control. Ocean surface displacement caused by submarine trailing vortices offers a potential means of detection by satellite photography. The stability and subsequent evolution of these vortices is therefore a matter of significant interest.

In a variety of vortical flows of practical interest, an ambient flow may be present that exhibits shear normal to the vortex axes. Common examples where the three-dimensional stability of vortices in cross-stream shear flows is important include three-dimensional interaction of coherent vortices in turbulent plane mixing layers or the formation of hairpins from transverse vortices in a turbulent boundary layer. Counter-rotating vortex pairs in the wake of lifting bodies also are frequently exposed to cross-stream shear in the ambient flow. For instance, aircraft trailing vortices may be subject to shear due to wind in the atmospheric boundary layer. Ship hull vortices may experience shear due to the wind-driven surface flow or to tidal flows.

The three-dimensional stability of vortices in shear flows has been studied previously via numerical computations by a number of investigators for the case of systems of nearly parallel vortices with the same circulation.[2–5] These papers demonstrate that a single vortex (or an array of like-signed vortices) immersed in a cross-stream shear flow exhibits an instability under certain conditions, due to its own self-induced velocity in the presence of the ambient shear, which may cause a perturbation to grow in a hairpin-like shape.

Although, in many of the examples noted above, there are other effects (e.g., the presence of a boundary, arrays of many vortices,

Received Feb. 2, 1996; revision received Oct. 18, 1996; accepted for publication Nov. 4, 1996.

*Associate Professor, Department of Mechanical Engineering; also Research Engineer, Iowa Institute of Hydraulic Research.

†Graduate Research Assistant, Department of Mechanical Engineering.

or nonuniform shear flow) that may influence the vortex motion, it is of value to specifically examine the effect of shear on three-dimensional vortex stability in the absence of such complications. The present paper is concerned with the effect of shear on the stability of a single vortex and of a pair of opposite-signed (counter-rotating) vortices for the case in which the ambient shear flow lies normal to the vortex axes (cross-stream flow) and in the plane of the vortex pair. We also have examined the case where the shear flow is oriented along the vortex axes, but have found no influence of the shear on the vortex stability in the linear theory for this case. Using a combination of theory and numerical calculations, we demonstrate that the presence of cross-stream shear has a strong quantitative effect on the regions of instability and growth rates of the unstable perturbations and causes dramatic qualitative changes to the nature of the instabilities observed.

In the absence of a cross-stream shear flow, the long-wave stability of a pair of counter-rotating vortices was previously examined by Raja Gopal[6,7] and Crow[8] using vortex filament theory, where the self- and mutually induced velocities of the vortices are obtained from the filament approximation to the Biot–Savart equation with cutoff of the singularity in the self-induced velocity. The linear theory was shown to remain valid well into the nonlinear regime in numerical computations by Moore.[9] Jimenez[10] showed that a pair of parallel (corotating) vortices is unconditionally stable in the linear theory. Extension of the linear theory to account for uniform axial flow in the vortex cores (which is a prominent feature of most wake vortices) was considered by Widnall and Bliss[11] and Moore and Saffman.[12] Robinson and Saffman[13] considered the three-dimensional stability of arrays of infinitely many parallel vortices, including the Karman vortex street and the symmetric double row. The long-wave stability theory for the counter-rotating vortex pair was further extended by Marshall,[14] who showed that stretching of the vortices along their axes (which is a prominent feature of turbulent hairpin vortices, for instance) leads to an eventual suppression of the instability in the linear theory, although for weak stretching rates the perturbations may grow substantially before decaying.

Whereas vortex filament theory predicts both a long- and short-wave instability for the vortex pair, the short-wave instability predicted by the filament theory (with no ambient shear or axial flow in the vortex core) is spurious and results from an incorrect expression for the self-induced velocity by the filament theory for $k\sigma = O(1)$. As shown by Moore and Saffman[15] and Tsai and Widnall[16] by analysis of the full Euler equations, the vortex pair does in fact exhibit a short-wave instability for wave numbers close to that for which the self-induced velocity of the second bending mode vanishes, whereas the filament theory only includes the first bending mode. The short-wave instability of the vortex pair is due to the straining flow exerted on each vortex of the pair by the presence of the other vortex, and is not significantly affected by small oscillations of the opposing vortex (for large values of bk). The most unstable perturbation is oriented along a line of vanishing azimuthal velocity and is carried outward by the radial component of the straining flow induced by the opposing vortex.[17] The short-wave instability was later applied to explain the instability of vortex rings by Widnall and Tsai.[18]

The problem of stability of a counter-rotating vortex pair immersed in a cross-stream shear flow thus involves a competition between the instability due to the mutually induced velocities of the vortices (for both long- and short-wave perturbations) and the instability due to the self-induced vortex motion in the presence of the cross-stream shear. To simplify this problem, it is convenient to assume (in the first two parts of the paper) that the shear flow is sufficiently weak that the vortex cores remain nearly circular. For small shear rates, it is also reasonable to assume that the stretching of vorticity associated with the background shear flow has a negligible effect on the vortex evolution.[2] For both of these reasons, we consider flows with shear rate S small compared to the average core vorticity $\Gamma/\pi\sigma^2$. So that the shear has a significant effect on the stability of a vortex pair, it is necessary that S be of the same order as or larger than the frequency $\Gamma/2\pi b^2$ associated with the mutual interaction of the vortices, where b is the nominal vortex separation distance. The present theory thus is concerned with cases with weak shear where the vortices are far apart in comparison to the core radius (i.e., $b/\sigma \gg 1$). Nonlinear computations are performed using vortex filament theory for long-wave perturbations and a three-dimensional vortex blob method (which is not restricted to weak background shear) for shorter wavelength perturbations and for higher shearing rates.

The linear stability theory for both a single vortex filament and a vortex pair in a background cross-stream shear are examined in Sec. II. Nonlinear computations for long-wave instability showing the effect of weak background shear are described in Sec. III. Nonlinear computations examining the validity of the theoretical results for medium-wavelength perturbations at moderate shearing rates are described in Sec. IV. Conclusions of the study are given in Sec. V.

II. Linear Stability Theory

In this section, we examine the linear stability of a single vortex of strength Γ and a vortex pair of opposite strengths $\pm\Gamma$ immersed in a cross-stream shear flow:

$$\boldsymbol{u}_E = Sz\boldsymbol{e}_y \tag{1}$$

where $\boldsymbol{e}_y$ is a unit vector in the y direction. The vortex axes are nominally aligned in the x direction, and the position vector to a point identified by the Lagrangian variable ξ on the vortex centerline C is denoted by $\boldsymbol{r}(\xi, t)$. For long-wave perturbations, the vorticity-induced velocity $\boldsymbol{u}_I$ of points on C is given by the filament approximation to the Biot–Savart equation,

$$\boldsymbol{u}_I(\xi, t) = -\frac{\Gamma}{4\pi}\int_{C[\delta_c]} \frac{\boldsymbol{r}-\boldsymbol{r}'}{|\boldsymbol{r}-\boldsymbol{r}'|^3} \times \frac{\partial \boldsymbol{r}'}{\partial \xi'}\,\mathrm{d}\xi' \tag{2}$$

where $\boldsymbol{r}' \equiv \boldsymbol{r}(\xi', t)$. The notation $C[\delta_c]$ implies that a segment of length $\delta_c\sigma$ is removed (or cut off) from the curve C on both sides of the singularity at $\boldsymbol{r} = \boldsymbol{r}'$, where the cutoff constant is given by[8]

$$\delta_c = \tfrac{1}{2}\exp(\tfrac{1}{4}) \approx 0.642 \tag{3}$$

for the case with uniform vorticity within the vortex core. The velocity $\boldsymbol{v} = \mathrm{d}\boldsymbol{r}/\mathrm{d}t$ of points on the vortex centerline is composed of the sum of the vorticity-induced velocity $\boldsymbol{u}_I(\xi, t)$ and a prescribed velocity field $\boldsymbol{u}_E(\xi, t)$. For the case with a vortex pair, $\boldsymbol{u}_I$ includes both the self-induced velocity of a vortex and the velocity induced by the opposing vortex of the pair.

For short-wave perturbations (with σk greater than about 0.5), the velocity induced by the opposing vortex of the pair still can be obtained from Eq. (2), provided that σ/b is small, but the filament approximation yields an incorrect solution for the self-induced velocity of the vortex. In the linear stability theory, the vortex is convected at a velocity that consists of the sum of the prescribed cross-stream shear flow, the velocity induced by the opposing vortex (for a vortex pair), and the self-induced velocity $u_\theta = \Omega_n(\delta)r$ due to the curvature of the vortex axis, where r is the displacement of the core centroid from the nominal vortex axis. For small-amplitude waves, the self-induced rotation rate can be obtained by numerical solution of the exact dispersion relationship for bending waves on a circular vortex core[12] for waves with any value of δ, and for long-wave perturbations yields results that approach those of the filament approximation (2).

Note that both the straining flow induced by the opposing vortex of the pair and the ambient shear flow will cause the vortex core to become slightly noncircular. For short-wave perturbations without shear flow, stability theories for a vortex in an ambient straining flow (which is used to simulate the effect of the opposing vortex of the pair) have been developed by Moore and Saffman[15] and Tsai and Widnall,[16] using an elliptical vortex core cross section as the basic state. The results of these analyses are extremely complicated, however, and would be considerably further compounded by the addition of a weak ambient shear. Comparing the results of the stability theories developed for a vortex of elliptical cross section to earlier results obtained using the dispersion relationship for a circular vortex core,[17] Tsai and Widnall[16] found that the results of the two theories are qualitatively consistent and yield short-wave stability results (e.g., growth rates, most unstable wave number)

that differ by less than 15%. The effects of elliptical core cross section, although not entirely negligible, thus seem not sufficiently important to warrant the complications introduced by its inclusion, at least for small shearing rates. This conclusion is further supported by comparison of the linear theory results to numerical solutions of the full Euler equations in Sec. IV.

A. Single Vortex in a Cross-Stream Shear Flow

The perturbations of the vortex occur in the y–z plane, such that the position of a point with axial location ξ on the filament is given by

$$\boldsymbol{r} = \xi \boldsymbol{e}_x + y(\xi, t)\boldsymbol{e}_y + z(\xi, t)\boldsymbol{e}_z \tag{4}$$

Using Eqs. (1) and (4), the evolution equations for the vortex axis are

$$\frac{\mathrm{d}y}{\mathrm{d}t} = u_2 + Sz, \qquad \frac{\mathrm{d}z}{\mathrm{d}t} = u_3 \tag{5}$$

We consider a harmonic perturbation on the vortex axis with wave number k, such that

$$y = \hat{y}(t)e^{ikz}, \qquad z = \hat{z}(t)e^{ikz} \tag{6}$$

For perturbations of the form (6) with infinitesimal amplitude, the Biot–Savart equation yields the self-induced velocity in the form[8]

$$u_2 = (\Gamma k^2/2\pi)\omega(\bar{\delta})z, \qquad u_3 = -(\Gamma k^2/2\pi)\omega(\bar{\delta})y \tag{7}$$

where $\bar{\delta} \equiv \delta_c \sigma k$. The self-induction function $\omega(\bar{\delta})$ is obtained from the filament equation (2), for long-wave perturbations, as

$$\omega(\bar{\delta}) \approx \frac{1}{2}\left[\frac{\cos\bar{\delta} - 1}{\bar{\delta}^2} + \frac{\sin\bar{\delta}}{\bar{\delta}} - Ci(\bar{\delta})\right] \tag{8}$$

where $Ci(\bar{\delta})$ is the cosine-integral. For small-amplitude perturbations, the self-induced rotation rate $\Omega_n(\delta)$ also can be obtained (for any value of δ) from solution of the exact dispersion relationship for bending waves on a circular vortex core[12]:

$$\frac{1}{c^2}\left[c\delta\frac{J_1'(c\delta)}{J_1(c\delta)} - \frac{2}{2\Omega_n^* - 1}\right] = -\delta\frac{K_1'(\delta)}{K_1(\delta)} \tag{9}$$

where

$$c^2 = \frac{4 - (2\Omega_n^* - 1)^2}{(2\Omega_n^* - 1)^2} \qquad \text{and} \qquad \Omega_n^* \equiv \frac{\pi\sigma^2\Omega_n}{\Gamma}$$

is a dimensionless self-induced rotation rate. The Bessel function $J_1(c\delta)$ has an infinity of roots for $c\delta > 0$, each of which yields a different solution (mode) for Ω_n^*, as indicated by the different values of n. The solutions for the first four modes are shown in Fig. 1. The dashed line in Fig. 1 indicates the value $\Omega_n^*(\delta)$ predicted by the result (8) of the filament theory, where $\Omega_n^*(\delta)$ and $\omega(\bar{\delta})$ are related by

$$\Omega_n^*(\delta) = -(\delta^2/2)\omega(\bar{\delta}) \tag{10}$$

Substituting Eqs. (6) and (7) into Eq. (5), the evolution equations for the vortex become

$$\frac{\mathrm{d}\hat{y}}{\mathrm{d}t} = \frac{\Gamma k^2}{2\pi}\omega(\bar{\delta})\hat{z} + S\hat{z}, \qquad \frac{\mathrm{d}\hat{z}}{\mathrm{d}t} = -\frac{\Gamma k^2}{2\pi}\omega(\bar{\delta})\hat{y} \tag{11}$$

The solution of Eq. (11) for $\hat{y}(t)$ and $\hat{z}(t)$ varies with time in proportion to $e^{\alpha t}$, where the dimensionless growth rate $\alpha^* \equiv \pi\sigma^2\alpha/\Gamma$ is given in terms of $\Omega_n^*(\delta)$ and the dimensionless shearing rate $S^* \equiv \pi\sigma^2 S/\Gamma$ by

$$(\alpha^*)^2 = \Omega_n^*(S^* - \Omega_n^*) \tag{12}$$

For $S^* = 0$, the coefficient α^* is imaginary for all values of δ, and the resulting perturbations are unconditionally stable. Regions of

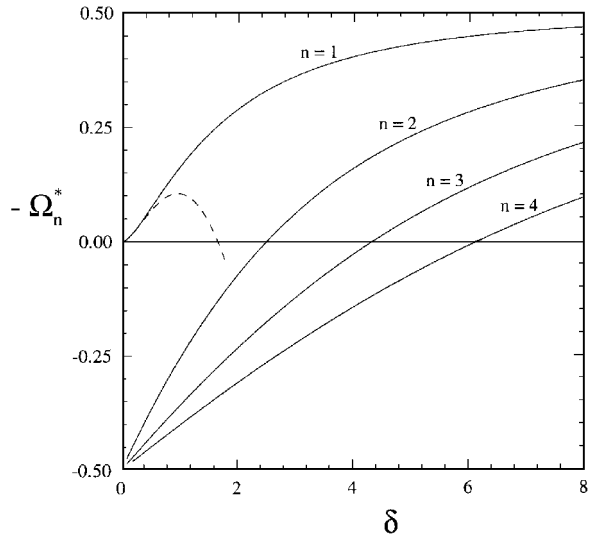

Fig. 1 Exact solution for self-induced rotation rate of a bending wave on a circular vortex core for the first-, second-, third-, and fourth-mode perturbations: dashed curve is the filament theory approximation for first-mode perturbations [obtained from Eqs. (7) and (8)].

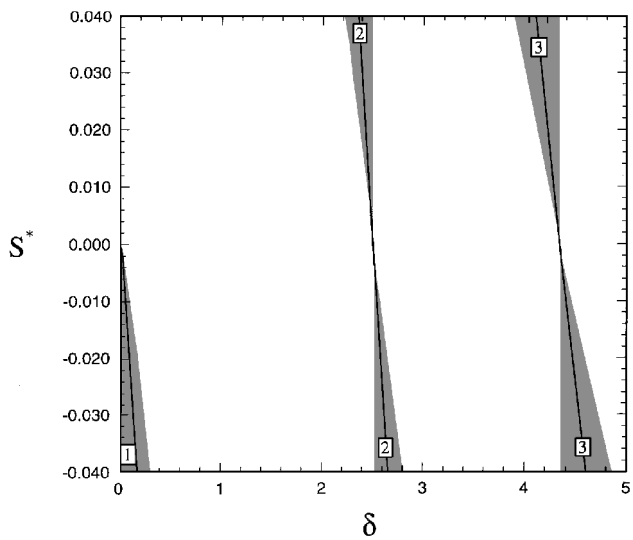

Fig. 2 Stability diagram for long-wave perturbations of a single vortex filament in a cross-stream shear flow: shaded and unshaded regions denote unstable and stable perturbations, respectively; boxed numbers indicate mode of solution for Ω_n from Eq. (9); dark curves denote the most unstable wave numbers, as predicted by Eq. (11).

unstable (shaded) and stable (unshaded) perturbations are shown on Fig. 2 in the space of δ and S^*. Boxed numbers are used throughout this section to designate instability regions for different modes of the solution for $\Omega_n^*(\delta)$ from Eq. (9). Because $\Omega_1^* < 0$ for all $\delta > 0$, the first mode exhibits unstable regions in Fig. 2 only for $S^* < 0$, such that the vorticity within the vortex has the same sign as that of the ambient shear flow. Higher-mode solutions exhibit instabilities for both positive and negative values of S^*, depending on whether the sign of $\Omega_n^*(\delta)$ is positive or negative, respectively.

The most unstable perturbation, with $\delta = \delta_f$, is obtained by maximizing $(\alpha^*)^2$ with respect to δ, which yields

$$\Omega_n^*(\delta_f) = \tfrac{1}{2}|S^*| \tag{13}$$

When Eq. (13) is satisfied, the self-induced rotation of the vortex is balanced by the rotation induced by the ambient shear flow, such that the perturbation grows at a constant angle of 45 deg to the direction of shear. Curves indicating the most unstable perturbations are plotted

in Fig. 2 for the first three modes. The dimensionless growth rate α_f^* for the most unstable perturbations is obtained from Eq. (12) as

$$\alpha_f^* = \tfrac{1}{2}|S^*| \tag{14}$$

B. Vortex Pair in a Cross-Stream Shear Flow

The position $\boldsymbol{r}_N(\xi_N, t)$ of a point ξ_N on vortex $N(=\{1, 2\})$ at time t is given by

$$\boldsymbol{r}_N = \xi_N \boldsymbol{e}_x + [(b/2)(-1)^N - (S\Gamma t^2/4\pi b) + y_N]\boldsymbol{e}_y + [-(\Gamma t/2\pi b) + z_N]\boldsymbol{e}_z \tag{15}$$

where b is the nominal separation distance between the two vortex filaments. The evolution equations for the vortex perturbations are

$$\frac{\mathrm{d}y_N}{\mathrm{d}t} = u_{N2} + Sz_N, \qquad \frac{\mathrm{d}z_N}{\mathrm{d}t} = u_{N3} \tag{16}$$

For harmonic, small-amplitude solutions for y_N and z_N of the form (6), the self- and mutually induced velocities are given by[8]

$$u_{12} = (\Gamma/2\pi b^2)[-z_1 + \psi(\beta)z_2 - \beta^2\omega(\bar{\delta})z_1] \tag{17a}$$

$$u_{13} = (\Gamma/2\pi b^2)[-y_1 + \chi(\beta)y_2 + \beta^2\omega(\bar{\delta})y_1] \tag{17b}$$

$$u_{22} = (\Gamma/2\pi b^2)[z_2 - \psi(\beta)z_1 + \beta^2\omega(\bar{\delta})z_2] \tag{17c}$$

$$u_{23} = (\Gamma/2\pi b^2)[y_2 - \chi(\beta)y_1 - \beta^2\omega(\bar{\delta})y_2] \tag{17d}$$

where $\beta \equiv kb$ and the mutual induction functions are defined by

$$\psi(\beta) = \beta^2 K_0(\beta) + \beta K_1(\beta), \qquad \chi(\beta) = \beta K_1(\beta) \tag{18}$$

Two modes of perturbation of the vortex pair, symmetric and antisymmetric, are defined, respectively, by

$$y_s = \frac{y_2 - y_1}{b}, \qquad z_s = \frac{z_2 + z_1}{b} \tag{19a}$$

$$y_A = \frac{y_2 + y_1}{b}, \qquad z_A = \frac{z_2 - z_1}{b} \tag{19b}$$

Four independent functions of β and δ are introduced as follows:

$$\begin{aligned} F_1 &= (\Gamma/2\pi b^2)[1 + \chi(\beta) - \beta^2\omega(\bar{\delta})] \\ F_2 &= (\Gamma/2\pi b^2)[1 - \psi(\beta) + \beta^2\omega(\bar{\delta})] \\ G_1 &= (\Gamma/2\pi b^2)[1 - \chi(\beta) - \beta^2\omega(\bar{\delta})] \\ G_2 &= (\Gamma/2\pi b^2)[1 + \psi(\beta) + \beta^2\omega(\bar{\delta})] \end{aligned} \tag{20}$$

The evolution equations for the symmetric and antisymmetric vortex perturbations can be written in terms of the functions (20) as

$$\frac{\mathrm{d}y_s}{\mathrm{d}t} = F_2 z_s + Sz_A, \qquad \frac{\mathrm{d}z_s}{\mathrm{d}t} = F_1 y_s \tag{21a}$$

$$\frac{\mathrm{d}y_A}{\mathrm{d}t} = G_2 z_A + Sz_s, \qquad \frac{\mathrm{d}z_A}{\mathrm{d}t} = G_1 y_A \tag{21b}$$

The presence of cross-stream shear causes a coupling between the symmetric and antisymmetric modes in Eqs. (21a) and (21b). The solution of Eqs. (21) for the symmetric and antisymmetric perturbations is proportional to $e^{\alpha t}$, where the growth rate α is given by

$$\alpha^2 = \tfrac{1}{2}(G_1G_2 + F_1F_2) \pm \tfrac{1}{2}[(G_1G_2 - F_1F_2)^2 + 4S^2G_1F_1]^{\frac{1}{2}} \tag{22}$$

Stability diagrams are obtained from Eq. (22) by varying the parameters β and δ/β for fixed values of the dimensionless shearing rate S^*. Because the symmetric and antisymmetric modes are coupled, there exist four solutions for α for each value of β and δ/β, which are given by $\pm\alpha^+$ when the positive sign is chosen in Eq. (22) and by $\pm\alpha^-$ when the negative sign is chosen. Stability

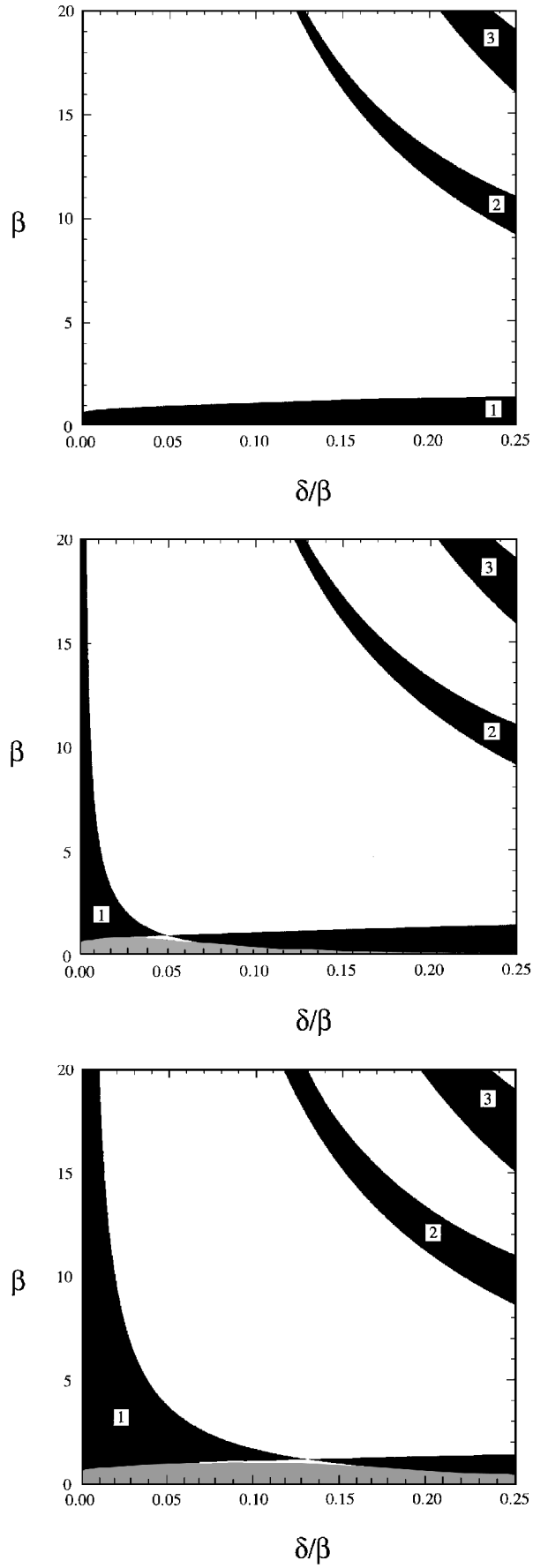

Fig. 3 Stability diagrams for a vortex pair in cross-stream shear, with dimensionless shear rates of a) $S^*= 0$, b) $S^*= 0.003$, and c) $S^*= 0.02$. [Boxed numbers indicate mode of solution for Ω_n from Eq. (9); dark-shaded regions along the δ/β axis and the β axis indicate regions of type A and B long-wave instabilities, respectively; gray-shaded regions indicate type C long-wave instability.]

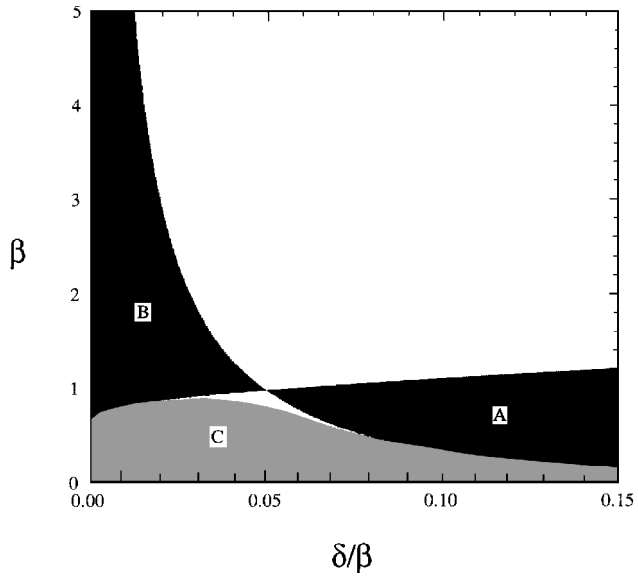

Fig. 4 Closeup stability diagram for long-wave perturbations, with types A, B, and C instabilities indicated by boxed letters. [All unstable regions are for the first-mode solution for Ω_n from Eq. (9).]

diagrams for α^+ with values of $S*$ of 0, 0.003, and 0.02 are shown in Figs. 3a, 3b, and 3c, respectively, for both long- and short-wave perturbations. Boxed numbers again are used to indicate the mode of solution for Ω_n. For $S* = 0$, instability of long-wave perturbations occurs in the first-mode solutions and instabilities of short-wave perturbations occur for second- and higher-order modes.[17] These instabilities are due to the mutual interaction between the two vortices of the pair. This region of instability is also apparent for cases with nonzero values of $S*$. Because several different instabilities occur for long-wave perturbations with $S* > 0$, we henceforth designate the instability associated with the region of long-wave instability in Fig. 3a (due to mutual vortex interaction) as type A instability.

An additional type of instability occurs in the presence of cross-stream shear flow due to the interaction of the self-induced velocity of the vortex with vorticity of the same sign as that of the shear flow with the ambient shear (as discussed in Sec. II.A). This shear-induced instability is indicated by dark-shaded regions along the β axis in Figs. 3b and 3c, which will henceforth be referred to as type B instability. The outer boundary of the type B instability occurs at a constant value δ_{crit} of δ, where δ_{crit} corresponds with the stability boundary in Fig. 2 (for the first mode) for the given value of $|S*|$.

As indicated in Fig. 2, the critical value of δ increases with increase in shear rate, such that the region of long-wave shear-induced instability increases progressively with $S*$ in Figs. 3b and 3c. Outside of the region where $\delta < \delta_{\text{crit}}$, the region of the long-wave type A instability does not appear to change with variation of shear rate. The intersection of the region of type A instability in Fig. 3a and the region $\delta < \delta_{\text{crit}}$, where we would expect type B instability to occur, results either in (surprisingly) stability of the vortex pair or in an entirely different type of instability, which will henceforth be referred to as type C instability and is denoted by gray-shaded regions in Figs. 3b and 3c. A closeup view of these three types of long-wave instabilities is given in Fig. 4 for $S* = 0.003$, and the three types of long-wave (first-mode) instabilities are designated by a boxed letter. Type C instability corresponds to cases where the term under the square root in Eq. (20) is negative, such that α^2 has both real and imaginary parts, whereas for both type A and type B instabilities α^2 is a positive real number. The stability diagrams for α^- include the type C instability (exactly as shown in the stability diagrams for α^+), but not the type A or B instabilities for long-wave perturbations.

Note that the stability of long-wave perturbations is dramatically affected by the presence of shear, even for extremely small values of the dimensionless shearing rate. The short-wave perturbations, on the other hand, are not as much affected by the shear flow until much larger values of $S*$. In Fig. 3, the shear seems to cause only a gradual thickening of the short-wave instability regions as $S*$ increases to about 0.02. As $S*$ increases further to about 0.1, the regions of short-wave instability are found to thicken very substantially, such that the instability regions for the second and third modes merge. For $S*$ greater than about 0.2, the vortex pair becomes unstable to nearly all wavelengths (such that instability diagrams of the form shown in Fig. 3 will be completely shaded). It is noted, however, that the present linear stability theory assumes circular vortex cores and may not be applicable for $S*$ values as large as 0.2.

The above theory can be further simplified in the limit of large β by noting that the mutual induction functions $\psi(\beta)$ and $\chi(\beta)$ approach zero in proportion to $\beta^{3/2}e^{-\beta}$ and $\beta^{1/2}e^{-\beta}$, respectively. Thus, for sufficiently large values of β these terms are negligible and the primary effect of the opposite vortex of the pair is simply to exert a straining flow, with strain rate $e = \Gamma/2\pi b^2$, centered at the nominal location of the given vortex.[15–17] Under this simplification, the expression (22) for growth rate reduces simply to

$$\alpha^2 = (e + \Omega_n)(e - \Omega_n \pm S) \tag{23}$$

The most unstable perturbations correspond to values of δ satisfying $\Omega_n(\delta_f) = |S|/2$, such that the growth rate of the most unstable perturbation is given by

$$\alpha_f = e + (|S|/2) \tag{24}$$

III. Nonlinear Evolution of Unstable Long-Wave Perturbations

For long-wave perturbations of the vortex pair in a weak cross-stream shear, the nonlinear vortex evolution is simulated using a filament theory in which the vortex is advected by the sum of the prescribed shear flow [Eq. (1)] and the velocity $\boldsymbol{u}_I$ induced by the vorticity field, obtained by numerical integration of the filament approximation of the Biot–Savart integral in the form

$$\boldsymbol{u}_I(\xi, t) = -\frac{\Gamma}{4\pi}\int_C \frac{\boldsymbol{r} - \boldsymbol{r}'}{(|\boldsymbol{r} - \boldsymbol{r}'|^2 + \mu^2)^{\frac{3}{2}}} \times \frac{\partial \boldsymbol{r}'}{\partial \xi'}\, d\xi' \tag{25}$$

The parameter μ serves to regularize the integral and is related to the core radius $\sigma(t)$ at time t by $\mu = 2\delta_R\sigma(t)$, where $\delta_R = (\frac{1}{2})\exp(-\frac{3}{4})$ is the Rosenhead cutoff for uniform vorticity within the core cross section. The core radius is assumed to be everywhere uniform, but to vary with time so as to maintain constant core volume. Core variation caused by differences in local stretching rates generate axial waves that act to eliminate the core area differences on a time scale much smaller than that of the lateral displacement of the vortex filament.[12,19]

It may be useful at this point to review the limitations that use of the vortex filament model, as given by Eq. (25), imposes on the numerical simulations in this section. It has been noted previously that the filament model applies only to cases in which the axial length scale of the vortex deformation is long compared to the core radius. From Fig. 1, we see that the filament approximation is suited only to cases with perturbations satisfying $\delta \lesssim 0.4$. A second restriction is that the filament approximation assumes that the vortex cores have circular cross-section, which requires both that the dimensionless shearing rate $S*$ is small (below about 0.1) and that the distance separating two filaments is sufficiently large compared to the core radius. Because for two vortices with opposite strength, the mutual straining of the vortices does not lead to core breakup until nearly the point at which the cores touch,[20] the filament approximation is commonly claimed to yield qualitatively accurate results until nearly up to the point of core touching.[9]

In the numerical simulations, the vortex pair is assumed to be periodic over a prescribed wavelength $\lambda = 2\pi/k$. Each of the vortex filaments are discretized into N sections over the computed period, with even increments in the Lagrangian variable ξ, and the Biot–Savart integral (25) is approximated using Simpson's rule. The calculations were advanced in time, with a fixed time step Δt, using the standard second-order predictor-corrector method and were stopped at the instant that the vortex cores touch. Symmetric perturbations

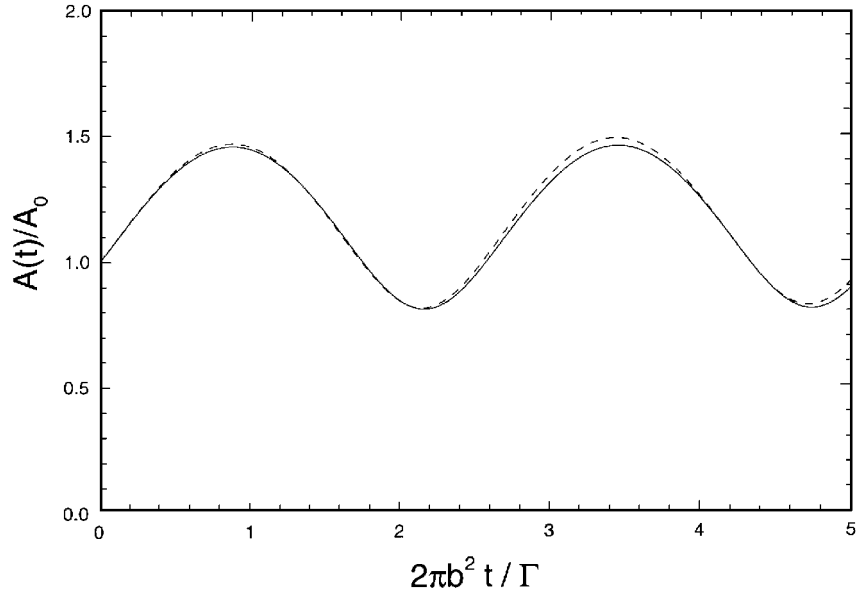

Fig. 5 Plot comparing the wave amplitude computed using the nonlinear vortex filament model (solid curve) to the theoretical result of Crow[8] (dashed curve) for a case with $\beta = 1.5$ and $\delta/\beta = 0.15$.

of the vortex filament were initially prescribed with amplitudes of 1% of the initial vortex separation distance and oriented at an angle of 45 deg to the nominal plane of the vortex pair.

A plot comparing the time variation of wave amplitude is given in Fig. 5 for a calculation in which three periods of the vortices are used in the Biot–Savart equation on each side of the computed section, the computed wavelength is discretized by 100 segments on each vortex, and the time step is set to $0.005(2\pi b^2/\Gamma)$. In this comparison, the computed wave amplitude is found to differ from the linear theory of Crow[8] by less than 2%. A series of calculations was performed to test the sensitivity of the numerical solutions to each of the three numerical parameters listed above. In these tests, runs were performed in which the number of periods of the vortex on each side of the computed section was increased to 5 and to 10, the time step was decreased to $0.002\,(2\pi b^2/\Gamma)$ and to $0.001(2\pi b^2/\Gamma)$ and the number of segments used to discretize the vortex was increased to 200. In all of these test calculations, the agreement with the theoretical predictions is similar to that shown in Fig. 5. The nonlinear calculations also were compared to results with a background shear flow using the linear theory in Sec. II, with similarly close agreement.

Results of computations showing the nonlinear evolution of the vortex pair are given in Figs. 6–8 for cases with long-wave instabilities of types A, B, and C, respectively. Plots are shown for projections in both the x–y and x–z planes, and only every other computational point is plotted. The three calculations shown here are all for a dimensionless shearing rate of $S* = 0.003$; however, a large number of other calculations have been performed with other values of the shearing rate. The vortex pair evolution has been found to exhibit similar characteristics for all points within a given instability region (as shown by the three regions in Fig. 4), whereas results for points in different instability regions are found to have striking qualitative differences.

Type A instabilities are driven by the interaction between the two vortices of the pair, and the shear has only a secondary effect on the perturbation after the amplitude becomes large. The result of a calculation typical of type A instabilities (for $\delta = 0.08$ and $\beta = 0.8$) is shown in Fig. 6. At small amplitude, the vortices have the form of the standard Crow instability,[8] with nearly symmetric perturbations that are aligned at an angle of about ± 45 deg relative to the nominal plane of the vortex axes. As the perturbation amplitude becomes larger, the shear flow has the effect of rotating the vortex system as a whole, such that the symmetry plane is no longer coincident with a plane $y = \text{const}$ but becomes tilted in the direction of the shear flow.

Type B instabilities are driven by interaction of the ambient shear flow with the one vortex of the pair that has vorticity oriented

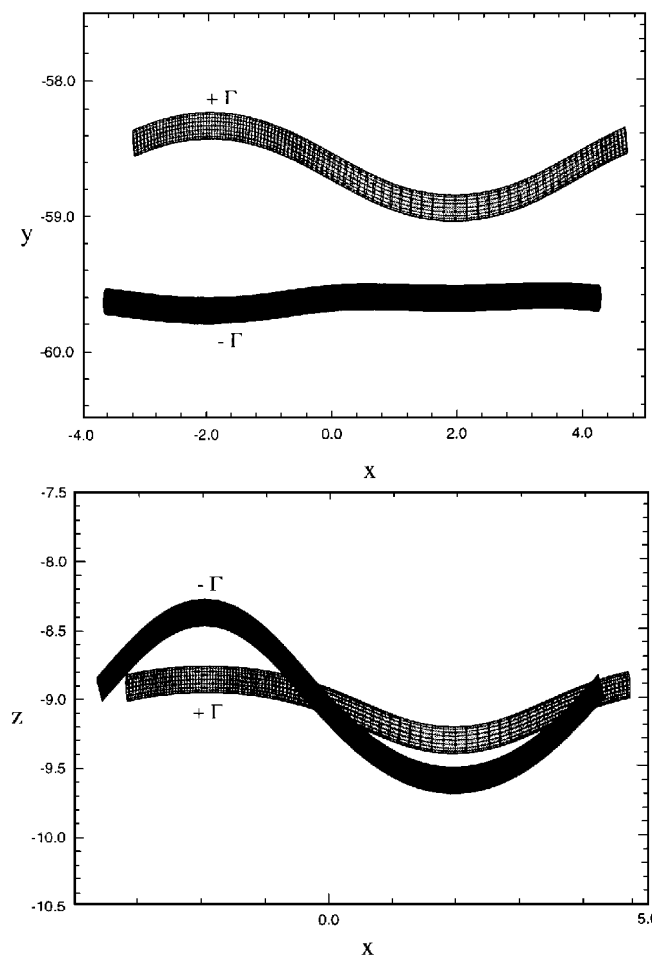

Fig. 6 Nonlinear evolution of a vortex pair undergoing type A long-wave instability for a case with $\delta = 0.08$, $\beta = 0.8$ and $S* = 0.003$. [The plot is shown at time $t = 9.0(2\pi b^2/\Gamma)$.]

nominally in the same direction as that of the cross-stream shear. The result of a calculation typical of type B instabilities (for $\delta = 0.03$ and $\beta = 1.5$) is shown in Fig. 7. Perturbations on the one vortex of the pair that is made unstable by the shear flow grow steadily, primarily in the direction of the shear flow. The other vortex of the pair initially remains fairly straight, but eventually exhibits waviness due to the induced velocity from large-amplitude perturbations

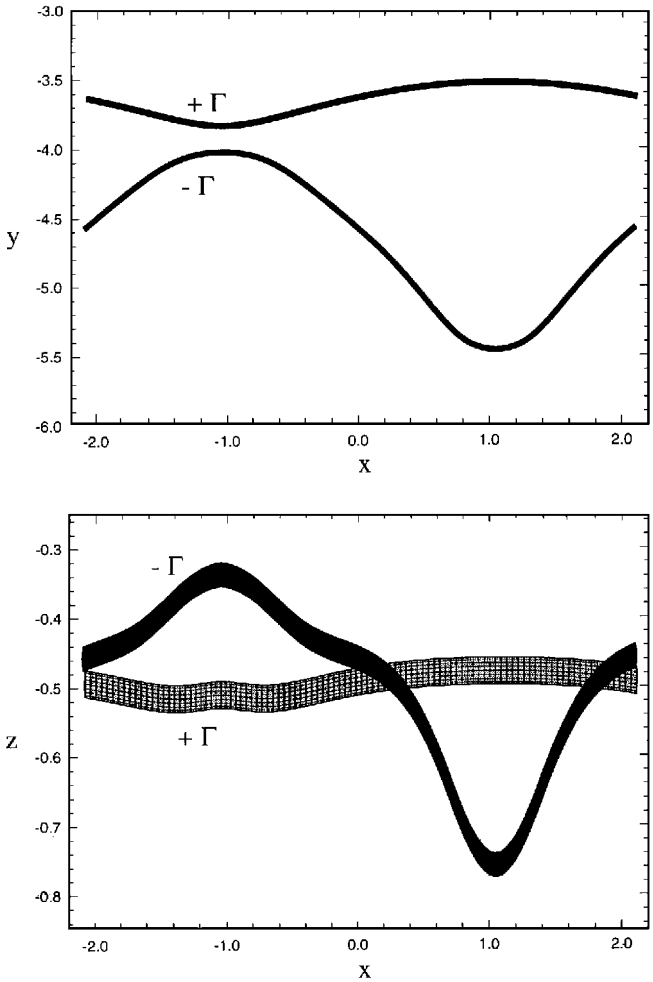

Fig. 7 Nonlinear evolution of a vortex pair undergoing type B long-wave instability for a case with $\delta = 0.03$ $\beta = 1.5$, and $S* = 0.003$. [The plot is shown at time $t = 0.5\,(2\pi b^2/\Gamma)$; the core radius appears smaller in the top plot because the vertical scale is much smaller than in the bottom plot; the apparent variation in core radius in the bottom plot is due to differences in the horizontal and vertical scales.]

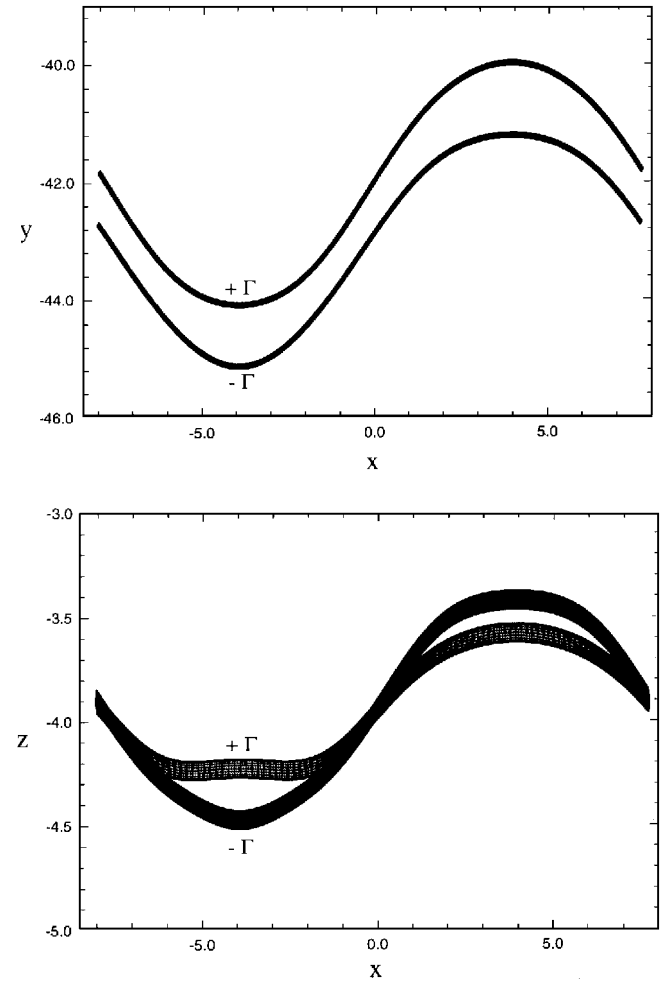

Fig. 8 Nonlinear evolution of a vortex pair undergoing type C long-wave instability for a case with $\delta = 0.02$, $\beta = 0.4$, and $S* = 0.003$. [The plot is shown at time $t = 3.8\,(2\pi b^2/\Gamma)$.]

of the opposing vortex. The resulting evolution of the pair is thus highly nonsymmetric, being dominated by the instability of only one of the vortices.

The evolution of a vortex pair with type C instability (in which both shear and interaction of the vortices are important) is shown in Fig. 8 (for $\delta = 0.02$ and $\beta = 0.4$) and is found to be quite different in appearance than that observed for either the type A or type B instabilities. Recall that the type C instability exhibits the same instability regions for both the α^+ and α^- eigenvalues (which correspond, respectively, to the growth rates of the symmetric and antisymmetric perturbations when no shear is present), whereas the type A and type B instabilities do not occur for the α^- eigenvalues. All calculations performed for type C instabilities exhibit strong antisymmetric perturbations, which typically dominate the vortex pair evolution, as shown in Fig. 8. The distance between the two vortices of the pair thus remains roughly uniform (until the perturbation amplitudes become very large), while the pair as a whole is deformed into an S-like shape that lies primarily in the x–y plane, but also exhibits a small amount of waviness when viewed in the x–z plane.

IV. Nonlinear Evolution of Unstable Perturbations at Moderate Shear Rates

The theoretical development and numerical calculations in the preceding sections assume that the effect of the ambient shear and the straining induced by the opposing vortex of the pair is sufficiently small that the vortex cross section can be treated as approximately circular. In this section, numerical computations are presented that seek to examine whether the principal results of the paper continue to hold, at least approximately, for a case in which the shear is sufficiently strong that the vortex cross section deviates substantially from a circular form.

Nonlinear evolution of the vortex perturbations is simulated by solution of the full Euler equations in the vorticity–velocity formulation using a type of Lagrangian vortex method developed by Marshall and Grant.[21] Computations using a viscous version of this method to solve the full Navier–Stokes equations, based on the diffusion approach of Marshall and Grant,[22] also were performed and compared to the inviscid results. For an inviscid flow, the evolution of the relative vorticity vector $\boldsymbol{\omega}$ is governed by the transport equation

$$\frac{\mathrm{d}\boldsymbol{\omega}}{\mathrm{d}t} = [(\boldsymbol{\omega} + \boldsymbol{W}) \cdot \nabla]\boldsymbol{u} \tag{26}$$

where $\boldsymbol{W} = -S\boldsymbol{e}_x$ is the vorticity of the ambient shear flow. The velocity vector $\boldsymbol{u}$ is obtained as the sum of the prescribed flowfield $\boldsymbol{u}_E$ and the vortex-induced velocity $\boldsymbol{u}_I$, which is given by the Biot–Savart integral

$$\boldsymbol{u}_I(\boldsymbol{x}, t) = -\frac{1}{4\pi}\int_V \frac{(\boldsymbol{x} - \boldsymbol{x}') \times \boldsymbol{\omega}(\boldsymbol{x}', t)}{|\boldsymbol{x} - \boldsymbol{x}'|^3}\,\mathrm{d}v(\boldsymbol{x}') \tag{27}$$

where V denotes the entire space occupied by the fluid and $\mathrm{d}v(\boldsymbol{x}')$ denotes an infinitesimal volume element in V.

In Lagrangian vortex methods, the vorticity is discretized by a set of N elements in order to evaluate the integral (27). The position of the control points (the element centroids) at time t is given by $\boldsymbol{x}_n(t)$, where $n = 1, \ldots, N$, and the control points are convected

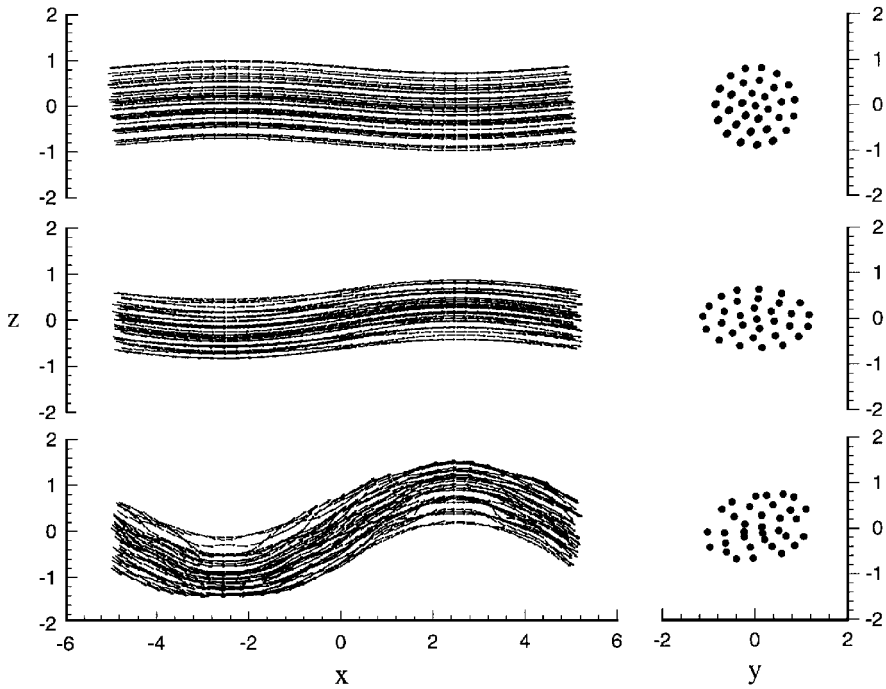

Fig. 9 Plot of the vorticity vector in the x–z plane, drawn at each internal control point, and the control point positions over a cross section of the vortex core in the y–z plane for a case with $S* = -0.2$ and $\delta = 0.63$ (the vortex is shown at dimensionless times $t* = 0$, 13.9, and 31.5).

by the flow as material points. The vorticity representation used to approximate the integral (27) has the form

$$\omega(\boldsymbol{x}, t) = \sum_{n=1}^{N} \boldsymbol{G}_n(t) f_n[\boldsymbol{x} - \boldsymbol{x}_n(t), R_n(t)] \tag{28}$$

The element amplitude vector $\boldsymbol{G}_n(t)$ represents the integral of the vorticity associated with the element over all space. The element weighting function f_n specifies the distribution of vorticity within the element. The weighting function is normalized such that its integral over all space is unity. The elements are overlapping Gaussians with radial length scale R_n, which is set to be about twice the distance between neighboring points.

With Gaussian weighting functions, the induced velocity at any point $\boldsymbol{x}$ in space is obtained as

$$\boldsymbol{u}_I(\boldsymbol{x}, t) = \sum_{n=1}^{N} \frac{P(\frac{3}{2}, |\boldsymbol{x} - \boldsymbol{x}_n|^2 / R_n^2)}{4\pi |\boldsymbol{x} - \boldsymbol{x}_n|^3} \boldsymbol{G}_n \times (\boldsymbol{x} - \boldsymbol{x}_n) \tag{29}$$

where $P(a, z)$ is the incomplete gamma function with limits $P = 0$ at $z = 0$ and $P = 1$ as $z \to \infty$ When $a = \frac{3}{2}$ and $z = x^2$, for some real variable x, a convenient expression for $P(\frac{3}{2}, x^2)$ is given in terms of the error function erf(x) as[23]

$$P\left(\frac{3}{2}, x^2\right) = \mathrm{erf}(x) - \frac{2xe^{-x^2}}{\sqrt{\pi}} \tag{30}$$

In standard vortex methods,[24] a constant volume h_n^3 is assigned to each element, such that the element amplitude is related to the value of the vorticity ω_n at the element control point by $\boldsymbol{G}_n = h_n^3 \omega_n$. Although this method is justified by formal convergence proofs,[25,26] the deformation of the original control-point arrangement by the flow can lead to accumulation of errors at large time, as originally noted by Beale.[27]

An alternative method in which the amplitudes are fit at each time step to the vorticity values at the control points, which are obtained from solution of Eq. (26), was suggested by Beale[27] and further developed by Marshall and Grant.[21] In the latter method, the amplitude fit is performed using the approximate iteration procedure

$$\omega(\boldsymbol{x}_m, t) = \boldsymbol{G}_m^{(q+1)} \sum_{n \in P(m)} W_{mn} + \sum_{n \in Q(m)} W_{mn} \boldsymbol{G}_n^{(q)} \tag{31}$$

where q is an iteration index. In this procedure, the amplitude is temporarily assumed to be constant over a set of points $Q(m)$ sufficiently close to the given point m. The set $P(m)$ is the complement of $Q(m)$ and $W_{mn} \equiv f_n(\boldsymbol{x}_n - \boldsymbol{x}_m)$. Procedure (31) typically is found to converge very quickly to a relative error of less than 10^{-6} (within about 6–15 iterations), and the number of iterations required for convergence seems to be independent of the number of control points. Further details about this procedure and validation tests are given by Marshall and Grant.[21,22]

Calculations using the inviscid vorticity-based method described above, with the amplitude-fitting procedure (31), were performed for a single vortex immersed in a background cross-stream shear flow. The initial perturbation in these calculations is a sine wave with amplitude of 20% of the nominal core radius aligned at an angle of 45 deg to the shear flow direction. Calculations were performed for cases with dimensionless shearing rates $S* = -0.2$ and -0.4 for both inviscid flow and viscous flow with a vortex Reynolds number $Re = 10^3$.

In these computations, the vorticity elements were placed in a series of planes spanning the cross section of the vortex: 35 computational points were placed in each plane inside the vortex core, with radius σ_0, and 85 computational points were placed in each plane in an annular region with radius $2\sigma_0$ surrounding the vortex core. The relative vorticity ω was initially prescribed to be uniform across the core cross section on the internal points and zero on the external points. At later times, the external points developed nonzero vorticity due to stretching of the vorticity associated with the background shear flow.

The value of Ω_I* corresponding to the fastest-growing mode-one perturbation is given by Eq. (13) as one-half of $S*$, and the corresponding value of δ for the fastest-growing wave is obtained from Fig. 1 as $\delta = 0.6$ for $S* = -0.2$ and as $\delta = 1.3$ for $S* = -0.4$. Using the nominal core radius σ_0, the perturbation wavelength is set as $\lambda / \sigma_0 = 10$ for $S* = -0.2$ and as $\lambda / \sigma_0 = 5$ for $S* = -0.4$, which in both cases is close to the fastest growing wave. For the case with $S* = -0.2$, the computations were performed with 40 cross-sectional planes (4800 elements) within the computed section and one period of the flowfield on each side of the computed section. For the case with $S* = -0.4$, the computations were performed with 20 planes (2400 elements) within the computed section and two periods on each side of the computed section. The time step was set adaptively, but maintained at less than $\Delta t* = 0.23$ for the

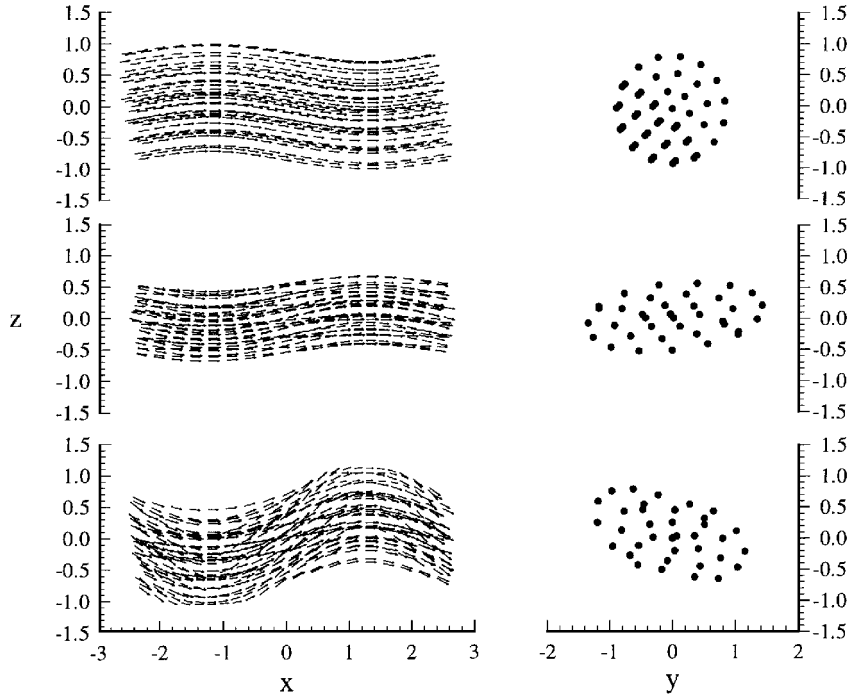

Fig. 10 Plot of the vorticity vector in the x–z plane, drawn at each internal control point, and the control point positions over a cross section of the vortex core in the y–z plane for a case with $S* = \pm 0.4$ and $\delta = 1.26$ (the vortex is shown at dimensionless times $t* = 0$, 5.3, and 11.1).

case with $S* = \pm 0.2$ and $\Delta t* = 0.15$ for the case with $S* = \pm 0.4$ (where $t* = \Gamma t/\pi\sigma^2$). A second-order predictor–corrector method was used to advance the solution in time. Short runs were performed with more periods and shorter time steps to ensure that the flow calculation is not significantly influenced by these parameters.

The element radius was held fixed at $R = 0.5\sigma_0$ for all elements during the computation. Whereas the computational points are placed within a region with nominal core radius σ_0 from the vortex axis, the vorticity field associated with these elements extends outward from the nominal core because of the finite thickness of the vorticity blobs. An effective core radius of the vortex, defined by the sum $\sigma_E = \sigma_0 + R$ of the nominal core radius and the average element radius, previously has been found to yield excellent agreement with theoretical results in a variety of test calculations.[22]

Computational results for cases with $S* = \pm 0.2$ and $S* = \pm 0.4$ are shown in Figs. 9 and 10, respectively, showing the vorticity vectors in the x–z plane (for each point internal to the core) and control point positions in the y–z plane within a cross section of the core at three different times. Although the core cross section is initially circular, it quickly deforms into a roughly elliptical shape, which rotates in the y–z plane while varying aspect ratio in an oscillatory manner similar to that described (in two dimensions) by Kida.[28] The maximum aspect ratio is about 1.7 for the case with $S* = \pm 0.2$ and 2.8 for the case with $S* = \pm 0.4$.

The perturbation along the axis of the vortex seems to become aligned primarily in the x–z plane and to grow in the z direction. The growth of the unstable perturbation is followed until the amplitude is four to five times the initial value. A plot showing the variation with time of the estimated wave amplitude for the two cases computed is given in Fig. 11. The solid and dashed curves in Fig. 11 are the best-fit exponential curves with amplitude starting at 20% of the nominal core radius σ_0. The outermost point for the case with $S* = \pm 0.2$ was not used in the curve fit, because the vortex evolution is highly nonlinear for this case. The coefficients of the exponential fits, denoted by $\alpha*_{\exp}$, are found to be 0.03 and 0.05 for the cases with $S* = \pm 0.2$ and $S* = \pm 0.4$, respectively, with an uncertainty of about 0.01 in both cases. Because the time $t*$ is nondimensionalized using the nominal core radius σ_0, we compare the product $\alpha*_{\exp}(\sigma_E/\sigma_0)^2$ with the theoretical prediction for a vortex with effective radius σ_E. The effective core radius for both computations is given by $\sigma_E = 1.5\sigma_0$ with an uncertainty of about $0.15\sigma_0$. The theoretical prediction was obtained by using Fig. 1 to find $\Omega*$ with δ based on the effective core

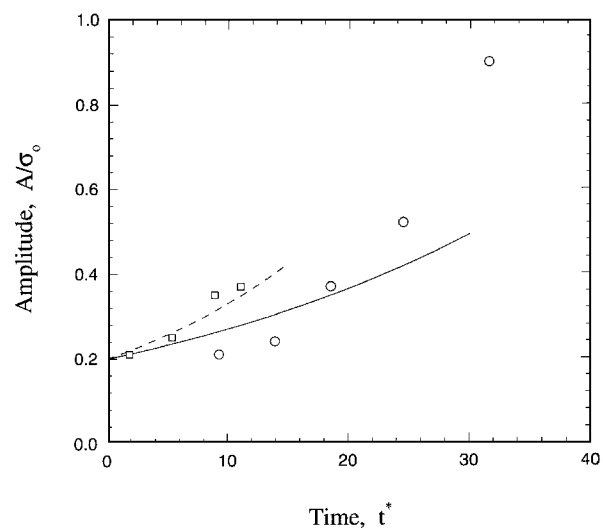

Fig. 11 Plot showing growth of perturbation amplitude with time for the computations illustrated in Figs. 9 and 10: the data are indicated by circles and squares, and best-fit exponential curves are indicated by a solid line and a dashed line for cases with $S* = \pm 0.2$ and $S* = \pm 0.4$, respectively.

radius σ_E and then using Eq. (12) to obtain the dimensionless growth rate $\alpha*$. For the case with $S* = \pm 0.2$, the theoretical prediction is $\alpha* = 0.087$ and the estimated value of the comparable quantity $\alpha*_{\exp}(\sigma_E/\sigma_0)^2$ from the computations is 0.068 ± 0.026. For the case with $S* = \pm 0.4$, the theoretical prediction is $\alpha* = 0.18$ and the estimated value of the comparable quantity $\alpha*_{\exp}(\sigma_E/\sigma_0)^2$ from the computations is 0.11 ± 0.03.

Considering the facts that the shear rate in the computations is not small and the core region exhibits considerable deformation, the computations are found to agree reasonably well with the theoretical predictions. We note also in this regard that Moore[29] found that a vortex ring with elliptical cross section propagates at a mean speed that is nearly the same as that of an equivalent ring (with the same core area and circulation) with circular cross-section, but experiences small, rapid oscillations in propagation speed because of the rotation of the elliptical core. It seems likely that a similar

situation might hold for the effect of core cross-section shape on the self-induced velocity of (long-wave) bending perturbations on otherwise straight vortices.

Near the end of the computations, the computational points external to the core begin to attain significant vorticity magnitudes through stretching of the vorticity field of the background shear flow. The background vorticity is initially aligned in the x direction, but with time becomes partially oriented in the y and z directions through the term $(\boldsymbol{W} \cdot \nabla)\boldsymbol{u}$ in Eq. (26) when the y and z components, v and w, of the vortex-induced velocity exhibit nonzero gradients in the x direction. These axial gradients of v and w arise because of the unstable axial perturbations of the primary vortex. The turning of the background vorticity in the y–z plane eventually leads to formation of wrapped vortex structures about the primary vortex, which stretch because of the induced flow from the primary vortex. The wrapped vortex structures grow progressively stronger with time until they finally disrupt the primary vortex core. All of the computational results reported in Figs. 9–11 are for times at which the wrapped vortex structures are weak and their effect on the vortex instability is negligible.

The viscous flow calculations, with $Re = 10^3$, exhibited similar results for the evolution of the vortex core as have been described in this section for the inviscid flow calculations, with the exception of a small growth in core radius of at most 20% of the initial radius during the course of the computations. The viscous calculations also yield vorticity structures in the external flow that wrap about the primary vortex, but the maximum vorticity within these structures is noticeably lower in the viscous flow calculations because of the effects of dissipation. The agreement between the viscous and inviscid flow calculations supports our claim that the stretching of the background vorticity field does not have a significant effect on the evolution of the primary vortex during the period for which the computational results are presented.

V. Conclusions

The paper examines instability of a counter-rotating vortex pair in the presence of cross-stream shear. For long-wave perturbations, it is found that three distinct types of instabilities occur. One type of instability is dominated by the mutual interaction of the two vortices of the pair, and the resulting evolution of the vortex pair appears as a nearly symmetric perturbation, in which the symmetry plane is rotated slightly by the ambient shear. A second type of instability is due to the interaction of the ambient cross-stream shear with the one vortex of the pair that has vorticity of the same sign as that of the shear flow. With this type of instability, one vortex of the pair becomes highly elongated by the shear flow, whereas the other vortex exhibits smaller (secondary) displacements due to the induced motion from the first vortex. In cases where both the mutual interaction of the vortices and the ambient shear flow would be expected to cause vortex instability, it is found that either the vortex pair will be stabilized or an entirely different, third type of instability will occur. With this third type of instability, the vortices evolve in an antisymmetric wave, in the form of a tilted S-shaped curve. It is found that the cross-stream shear will have a profound effect on the long-wave evolution of the vortex pair, for cases with sufficiently small values of σ/b, even when the shear rate is an extremely small fraction (e.g., less than 0.1%) of the average vorticity within the vortex core.

For short-wave instabilities, the presence of cross-stream shear is found to have very little effect on the stability of the vortex pair, aside from a slight widening of the bands of unstable wave numbers, until the shearing rate exceeds about 5% of the average vortex vorticity.

The conclusions of this paper are restricted to shearing rates that are sufficiently small that the deviation of the vortex cross-section from a circular shape can be neglected. Numerical computations of the instability of a single vortex in a shear flow with moderate shear rates indicate that the theoretical stability results (at least for a single vortex) continue to hold qualitatively even for shear rates that are not infinitesimal. This result suggests that the stability of a vortex due to interaction with a cross-stream shear may not be very sensitive to deformation of the vortex core, provided that the shearing rate is not so large as to cause the core shape to spread out into a thin sheet.

Finally, for an unstable vortex at moderate shearing rates, the background shear flow stretches (because of the wave motion on the primary vortex) and becomes partially oriented in the cross-sectional plane of the primary vortex, forming vortex structures that wrap about the primary vortex core. These structures also stretch out in the direction of the shear flow, becoming progressively stronger in time and eventually disrupting the primary vortex core.

Acknowledgments

Funding was provided by the U.S. Army Research Office under Grant DAAH04-96-1-0081. The Program Monitor was Thomas Doligalski. Supercomputer time was provided by the San Diego Supercomputer Center. The authors are grateful to John R. Grant for suggesting this problem and for discussions during the course of the study.

References

[1]Saffman, P. G., *Vortex Dynamics*, Cambridge Univ. Press, Cambridge, England, UK, 1992.

[2]Aref, H., and Flinchem, E. P., "Dynamics of a Vortex Filament in a Shear Flow," *Journal of Fluid Mechanics*, Vol. 148, 1984, pp. 477–497.

[3]Ashurst, W. T., and Meiburg, E., "Three-Dimensional Shear Layers Via Vortex Dynamics," *Journal of Fluid Mechanics*, Vol. 189, 1988, pp. 87–116.

[4]Corcos, G. M., and Lin, S. J., "The Mixing Layer: Deterministic Models of a Turbulent Flow, Part 2: The Origin of the Three-Dimensional Motion," *Journal of Fluid Mechanics*, Vol. 139, 1984, pp. 67–95.

[5]Pierrehumbert, R. T., and Widnall, S. E., "The Two- and Three-Dimensional Instabilities of a Spatially Periodic Shear Layer," *Journal of Fluid Mechanics*, Vol. 114, 1982, pp. 59–82.

[6]Raja Gopal, E. S., "Motion and Stability of Vortices in a Finite Channel: Application to Liquid Helium II," *Annals of Physics* (New York), Vol. 25, 1963, pp. 196–220.

[7]Raja Gopal, E. S., "Oscillations of Quantized Vortices in Rotating Liquid Helium II," *Annals of Physics* (New York), Vol. 29, 1964, pp. 350–365.

[8]Crow, S. C., "Stability Theory for a Pair of Trailing Vortices," *AIAA Journal*, Vol. 8, No. 12, 1970, pp. 2172–2179.

[9]Moore, D. W., "Finite Amplitude Waves on Aircraft Trailing Vortices," *Aeronautical Quarterly*, Vol. 23, 1972, pp. 307–314.

[10]Jimenez, J., "Stability of a Pair of Co-Rotating Vortices," *Physics of Fluids*, Vol. 18, No. 11, 1975, pp. 1580, 1581.

[11]Widnall, S. E., and Bliss, D. B., "Slender-Body Analysis of the Motion and Stability of a Vortex Filament Containing an Axial Flow," *Journal of Fluid Mechanics*, Vol. 50, Pt. 2, 1971, pp. 335–353.

[12]Moore, D. W., and Saffman, P. G., "The Motion of a Vortex Filament with Axial Flow," *Philosophical Transactions of the Royal Society of London, Series A: Mathematical and Physical Sciences*, Vol. 272, 1972, pp. 403–429.

[13]Robinson, A. C., and Saffman, P. G., "Three-Dimensional Stability of Vortex Arrays," *Journal of Fluid Mechanics*, Vol. 125, 1982, pp. 411–427.

[14]Marshall, J. S., "The Effect of Axial Stretching on the Three-Dimensional Stability of a Vortex Pair," *Journal of Fluid Mechanics*, Vol. 241, 1992, pp. 403–419.

[15]Moore, D. W., and Saffman, P. G., "The Instability of a Straight Vortex Filament in a Strain Field," *Proceedings of the Royal Society of London, Series A: Mathematical and Physical Sciences*, Vol. 346, 1975, pp. 413–425.

[16]Tsai, C. Y., and Widnall, S. E., "The Stability of Short Waves on a Straight Vortex Filament in a Weak Externally Imposed Strain Field," *Journal of Fluid Mechanics*, Vol. 73, Pt. 4, 1976, pp. 721–733.

[17]Widnall, S. E., Bliss, D. B., and Tsai, C. Y., "The Instability of Short Waves on a Vortex Ring," *Journal of Fluid Mechanics*, Vol. 66, Pt. 1, 1974, pp. 35–47.

[18]Widnall, S. E., and Tsai, C. Y., "The Instability of the Thin Vortex Ring of Constant Vorticity," *Philosophical Transactions of the Royal Society of London, Series A: Mathematical and Physical Sciences*, Vol. 287, 1977, pp. 273–305.

[19]Marshall, J. S., and Grant, J. R., "Evolution and Breakup of Vortex Rings in Straining and Shearing Flows," *Journal of Fluid Mechanics*, Vol. 273, Aug. 1994, pp. 285–312.

[20]Saffman, P. G., and Tanveer, S., "The Touching Pair of Equal and Opposite Vortices," *Physics of Fluids* (New York), Vol. 25, No. 11, 1982, pp. 1929, 1930.

[21]Marshall, J. S., and Grant, J. R., "Penetration of a Blade into a Vortex Core: Vorticity Response and Unsteady Blade Forces," *Journal of Fluid Mechanics*, Vol. 306, Jan. 1996, pp. 83–109.

[22]Marshall, J. S., and Grant, J. R., "A Lagrangian Vorticity Collocation Method for Viscous, Axisymmetric Flows With and Without Swirl," *Journal of Computational Physics* (submitted for publication).

[23] Abramowitz, M., and Stegun, I. A., *Handbook of Mathematical Functions*, Dover, New York, 1965.

[24] Leonard, A., "Computing Three-Dimensional Incompressible Flows with Vortex Elements," *Annual Review of Fluid Mechanics*, Vol. 17, 1985, pp. 523–559.

[25] Beale, J. T., and Majda, A., "Vortex Methods, Pt. 1: Convergence in Three Dimensions," *Mathematical Computations*, Vol. 39, 1982, pp. 1–27.

[26] Anderson, C., and Greengard, C., "On Vortex Methods," *SIAM Journal of Numerical Analysis*, Vol. 22, 1985, pp. 413–440.

[27] Beale, J. T., "On the Accuracy of Vortex Methods," *Proceedings of the Workshop on Computational Fluid Dynamics and Reacting Gas Flows*, I.M.A., Univ. of Minnesota, Minneapolis, MN, 1986.

[28] Kida, S., "Motion of an Elliptic Vortex in a Uniform Shear Flow," *Journal of the Physical Society of Japan*, Vol. 50, No. 10, 1981, pp. 3517–3520.

[29] Moore, D. W., "The Velocity of a Vortex Ring with a Thin Core of Elliptical Cross Section," *Proceedings of the Royal Society of London, Series A: Mathematical and Physical Sciences*, Vol. 370, 1980, pp. 407–415.